Control of a Segmented Three-Phase Synchronous Motor with Highly Coupled Sub-Windings

Antoine Cizeron, Javier Ojeda, Eric Monmasson, Olivier Béthoux

DOI: 10.1109/TIE.2022.3183342

Publisher: IEEE

To appear in: ***Transactions on Industrial Electronics***

Received date: October 26, 2021

Revised date: February 8, 2022 and April 29, 2022

Accepted date: June 6, 2022

Date of Publication: Available online 21 Juin 2022 (Early Access)

Please cite this article as:

A. Cizeron, J. Ojeda, E. Monmasson and O. Béthoux, "Control of a Segmented Three-Phase Synchronous Motor with Highly Coupled Sub-Windings," in *IEEE Transactions on Industrial Electronics*, 2022, doi: 10.1109/TIE.2022.3183342.

Document Version: Early version, before edition, also known as pre-print

Control of a Segmented Three-Phase Synchronous Motor with Highly Coupled Sub-Windings

Antoine Cizeron, Javier Ojeda, *Member, IEEE*,
Eric Monmasson, *Senior Member, IEEE*, and Olivier Béthoux

***Abstract*—This article addresses the control issue of a structure enabling the segmentation of three-phase electric drives. The proposed segmentation process offers an additional degree of freedom in terms of voltage rating for power electronics but results in a three-phase system with highly coupled sub-windings. Thus, for such a segmented motor, the true challenge lies in controlling the machine global electromagnetic torque while balancing the power among the different inverters. To tackle this issue, the dq standard synchronous frame is extended to common and differential modes. This approach enables to design a suitable control structure based on an analytical model and physical considerations. The developed model is calibrated with realistic numerical values obtained from a finite element analysis. Finally, an experimental setup allows developing a proof of concept which shows the interest of the proposed control method compared to a standard multiple dq-frame method. The key finding is that the above-mentioned control objective of the segmented synchronous motor can be achieved without additional inductors and despite the severe constraint imposed by such highly coupled segmentation.**

***Index Terms*—AC motor drives, segmented motor drives, highly coupled segmentation.**

I. Introduction

THE current trend in transport electrification is to supply the electric motor drives with a DC bus voltage of several hundred Volt. It induces electrical risks to persons and requires complex insulation monitoring [1]. Lowering the electric drives voltages down to 48V standard drastically mitigates electrical hazards, which is of particular benefit to transportation applications. It also significantly reduces the insulation system stress [2] and enables using silicon MOSFETs or wide band-gap technologies, both having low switching and conduction losses [3], [4]. For a given three-phase motor and a given current rating, it is possible to reduce the voltage rating by using several independently supplied winding sets [5]. These structures, often referred to as segmented drives, are also relevant approaches in ensuring continuity of service and enhancing drive energy efficiency since each phase is made of several sub-windings [6]. Improvements in connector technology [7], [8] as well as the attractive benefit of integrating power converters close to the motor end windings [3], [9], [10] highly mitigate the drawback of modular structures, namely the increased number of terminals. On the basis of these considerations, a recent patent [11] suggests the innovative Highly Coupled Segmentation (HCS) of motor drive structures. It opens up the possibility of dramatically lowering the drive voltage rating. However, it also induces high magnetic coupling between each winding sets [12] and may challenge the related torque and flux control structure. The key point of this article is to demonstrate that this issue can be addressed by an appropriate controller.

Among the numerous ways to obtain multiple three-phase winding sets, two categories can be distinguished [13] and are compared in Table I. The first category concerns the multiphase motor having $k \times 3$ phases (MK3P) which can be split in k three-phase winding sets with different phase angles [14]–[17]. Most of the MK3P drives require an individual design of a specific multiphase motor and a multiphase control frame. The main expected benefit is a reduced torque ripple [10], [18]. However, the open-circuit fault of a winding set influences the torque harmonics and requires a dedicated fault-tolerant structure [17]. The second category corresponds to the segmented drives, which are obtained through the reconfiguration of the windings of an existing three-phase stator in several independant winding sets [3], [19]–[21]. The aim of the segmentation approach is to enable an effective drive resilience, an efficient drive power sharing and a reduced power supply voltage. In this context, the only requested constraint is to keep the torque ripples similar to the one produced by the initial three phase motor (without segmentation of its stator windings) driven by its conventional inverter. This category is declined into two segmentation processes in Table I.

Multi-Sector Segmentation (MSS) layout is the standard approach in segmenting the windings of a three-phase motor. Each elementary three-phase winding set is housed in a distinct stator sector [6], [21], [25]–[27]. As any other segmentation process, the MSS approach induces no change in the motor

Manuscript received October 26, 2021; revised February 8, 2022; accepted June 6th, 2022.

A. Cizeron and O. Béthoux are with the Laboratoire de Génie Electrique et Electronique de Paris, 91192, Gif-sur-Yvette, France. (e-mail: antoine.cizeron@geeps.centralesupelec.fr).

J. Ojeda and E. Monmasson are with the Systèmes et Applications des Technologies de l'Information et de l'Energie laboratory, 91192, Gif-sur-Yvette, France.

10.1109/TIE.2022.3183342

TABLE I: Comparison of electric machines based on multiple three-phase winding sets.

Objectives \ Subdivision types	MK3P	Segmentation processes	
		MSS	HCS
Power-sharing capability	✓ [14]	✓ [6]	✓ [11]
Degraded mode operation (open-circuit fault of a subdivision)	✗ (Requires harmonic control [17])	✗ (Requires radial force control [22])	✓
Torque harmonics reduction	✓ [23]	✗	✗
Maximum segmentation level	Number of three-phase winding sets	Number of poles per phase	Number of turns per phase [11]
Interleaved PWM implementation	✓ [10]	✓ [21]	✗ (Requires external coupler [24])
Feed forward compensation	Matrix with MDQF [14]	Scalar with MDQF [21]	Matrix with MDQF, Scalar with the proposed CDM method

low harmonic torque ripple distribution [21] while enabling the parallelization of low voltage DC sources [3]. However, an additional radial force control is required in the MSS structure in order to take advantage of its power sharing capability [6] or to implement a fault-tolerant scheme [22]. Moreover, the MSS approach is limited by the number of poles per phase N_p. Consequently, it cannot adapt all electrical machine to a low voltage standard specification.

A recent international patent suggests an alternative segmentation option enabling to extend the drive modularity level up to the theoretical limit of the winding turn [11]. As such, this innovative architecture, referred to as the HCS, allows a full degree of freedom in the sizing of current and voltage ratings [28], [29]. It also facilitates the integration of the power converters close to the motor windings, thus limiting electromagnetic compatibility issues and boosting inverters heat power transfer. Since the number of turns per phase N_t is usually higher than the number of poles per phase N_p, the HCS is significantly more flexible than the MSS and enables using low voltage power supply for almost any electric drive. To enlighten their differences in terms of magnetic configuration and control strategy, the MSS and HCS layouts are both implemented on an existing three-phase Hybrid Excitation Flux Switching Machine (HEFSM). The choice of the hybrid motor topology is only due to laboratory availability. The HCS approach can easily be adapted to any kind of synchronous motor since it has already been used to achieve an on-board 3-phase charger in an electrical vehicle [13], [29] and to mitigate the Pulse Width Modulation (PWM) noise [24].

Concerning the control of a segmented motor, the Multiple dq-Frame (MDQF) method independently treats each elementary winding set. It can easily be used to control the MSS structure since its magnetic couplings are low between different sectors [21]. However, contrary to the MSS structure, the HCS structure presents large mutual inductances between each winding set. They are namely in the order of their self inductances [29], which is specific regarding the other segmented drives [19]–[21] and mars the effectiveness of the feed forward compensation, even in a healthy mode (Table I). As a matter of fact, the traditional MDQF control structure requires to combine the HCS structure with additional external coupled inductors [24]. Then, for reasons of cost, performance and space, the present article focuses on the feasibility of controlling the HCS structure without any additional coupled inductors and proposes an adapted Common and Differential Mode (CDM) control scheme, based on physical considerations, and easy to design and tune.

The main contributions of the paper are:

1) an in-depth analysis of the magnetic specificity of the proposed HCS structure.
2) a comparison between MSS and HCS structures based on inductance measurements.
3) the analysis, design and tuning of a dq-based CDM controller applied to a segmented three-phase synchronous motor with HCS structure.
4) an experimental validation as a proof of concept of the proposed CDM controller and its comparison with the MDQF control, both implemented on the HCS structure.
5) an experimental demonstration of the promising capability of the CDM controller in terms of power-sharing between inverters, even in case of faulty operation.

The rest of this paper is organized as follows. Section II introduces the HCS configuration in comparison with the well-known MSS approach. Using Finite Element Analysis (FEA), it assesses the coupling value of the 3-phase motor sub-windings for both HCS and MSS approaches. It hence permits to highlight the need to set up a specific control law based on a dedicaded transform applied in the rotating dq-frame. In section III, the dq-based suggested components are investigated in details and then the suggested control architecture is described. Section IV reports the experimental results obtained using a laboratory setup based on a $1\ kW$ HCS drive. Finally, section V provides conclusions and perspectives.

II. Comparison of MS and HC approaches

A. Three-phase motor segmentation

Based on an already existing conventional three-phase electric drive (Fig. 1), segmenting the initial windings in multiple electrically independent winding sets provides an attractive mean to lower the electric drive rated voltage. An elementary winding set is made of three sub-windings belonging to different phases and is powered by its dedicated inverter. The elementary winding set and its associated inverter constitute an elementary drive. The number of elementary drives is called

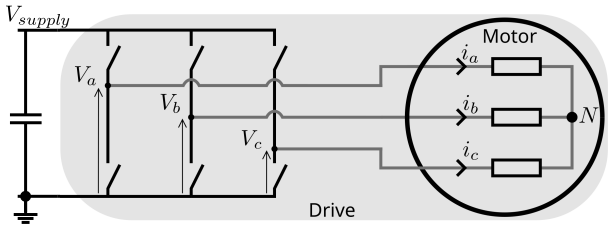

Fig. 1: Conventional drive of a three phase motor.

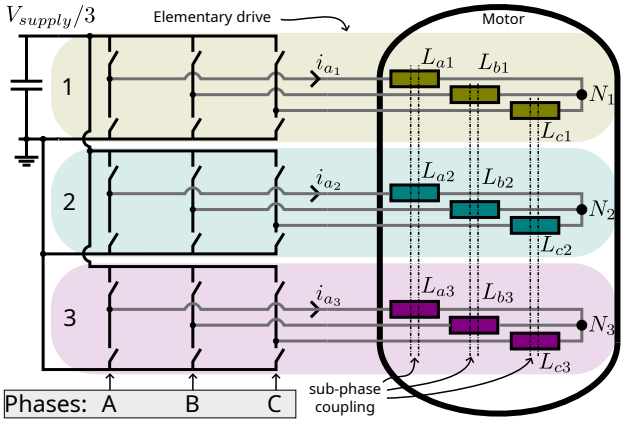

Fig. 2: The reduced voltage power supply of a segmented motor in the case of $N_{sc} = 3$ elementary drives.

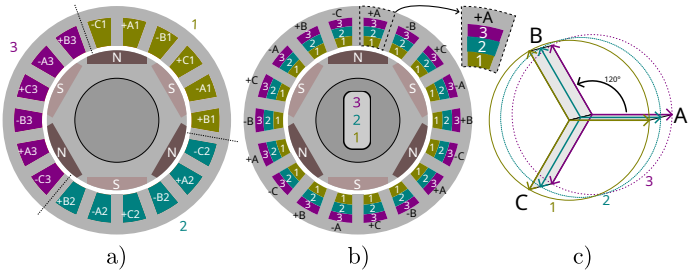

Fig. 3: Three poles pairs, three-phase motor with sub-windings corresponding to a) the MSS layout, b) the proposed HCS layout and c) their corresponding electrical angles.

the scaling factor, defined as N_{sc}. In this context, the electric motor is driven by several independent inverters as illustrated in Fig. 2 for the specific case of $N_{sc} = 3$. The segmented power supply has to produce in the air-gap the same global magnetomotive force (mmf) than the original power supply (Fig. 1). Thereby, based on Ampere law, each elementary drive conducts the initial motor rated current while the Faraday law shows that their rated voltage is N_{sc} times smaller than in the initial drive.

In this paper, the control issue of the studied HCS approach is compared with the one of the standard MSS method. Fig. 3a and 3b show the spatial stator layouts of the MSS and the HCS structures, respectively. Obviously the innovative HCS layout is more flexible than the MSS segmentation one and could lead to an ultimate voltage reduction when each turn has its own inverter. As the electrical phase shift between sub-windings of a single phase is zero for both cases, the N_{sc} electric angles of each structure is set to an identical control value. An ordinary PWM technique is implemented [30]. Moreover, a common PWM carrier is used for the N_{sc} elementary drives [12]. The key control difference between the two approaches lies in the coupling factor between sub-windings of the same phase, represented by double dotted lines in Fig. 2. It is low in the MSS structure [21] and high in the HCS structure [12].

B. Machine modelling in the rotating dq-frame

To design the control of the different elementary winding sets, a low frequency model has to be defined. It is hence based on the phenomena involved at the fundamental frequency. Magnetic saturation, saliency and iron losses are not taken into account. The considered segmentation process of $N_{sc} = 3$ elementary drives (Fig. 3) results in a total of $3N_{sc} = 9$ sub-windings in both configurations. Each sub-winding has its own voltage equation based on Faraday's law. The related $3N_{sc}$ equations lead to the following dynamical model

$$\mathbf{V} - \mathbf{V}_N = [\mathbf{R}] \cdot \mathbf{I} + [\mathbf{L}] \cdot \frac{d\mathbf{I}}{dt} + \mathbf{E} \tag{1}$$

where $[\mathbf{R}]$ is a diagonal matrix containing the resistive terms of each sub-winding. As the number of turns, and consequently the conductor length, is the same for each elementary sub-winding, it is assumed that this term presents insignificant discrepancies between all the sub-windings. Thus, the resistance term is considered as a scalar R in the different frame. $\mathbf{V}$ are the voltages applied at the middle point of the inverter legs while $\mathbf{V}_N$ are the voltages of the related neutral points. $\mathbf{I}$ is the sub-winding current vector and $\mathbf{E}$ is the back-emf term.

The structure of the inductance matrix $[\mathbf{L}]$ could be simplified by using a proper ordering. Within the matrix expression, the sub-windings are ordered by their elementary drive number (Fig. 2) and then by their phase one. Hence, the vector $\mathbf{X}$ in the natural frame includes the following $3N_{sc}$ components

$$\mathbf{X} = \begin{pmatrix} x_{a1} & x_{a2} & x_{a3} & x_{b1} & x_{b2} & x_{b3} & x_{c1} & x_{c2} & x_{c3} \end{pmatrix}^T. \tag{2}$$

Based on this ordering method, the resulting inductance matrix $[\mathbf{L}]$ is arranged as a conventional three-phase structure. Equation (3) shows the equivalent three-phase inductance matrix for the considered segmented winding layouts (Fig. 3)

$$[\mathbf{L}] = \begin{pmatrix} [\mathcal{L}_a] & [\mathcal{M}_{ab}] & [\mathcal{M}_{ac}] \\ [\mathcal{M}_{ba}] & [\mathcal{L}_b] & [\mathcal{M}_{bc}] \\ [\mathcal{M}_{ca}] & [\mathcal{M}_{ba}] & [\mathcal{L}_c] \end{pmatrix} \tag{3}$$

where $[\mathcal{L}_a]$ is a $(N_{sc} \times N_{sc})$ matrix containing the self-inductances of each sub-winding of phase a and the mutual inductances representing the magnetic coupling among them. It is assumed that all phases are symmetric, so the self-inductance matrices are equal to $[\mathcal{L}_s]$ and the mutual inductance matrices are equal to $[\mathcal{M}_s]$. In this way, the inductance matrix becomes

$$[\mathbf{L}] = \begin{pmatrix} [\mathcal{L}_s] & [\mathcal{M}_s] & [\mathcal{M}_s] \\ [\mathcal{M}_s] & [\mathcal{L}_s] & [\mathcal{M}_s] \\ [\mathcal{M}_s] & [\mathcal{M}_s] & [\mathcal{L}_s] \end{pmatrix}. \tag{4}$$

The dq transformation is applied to each of the N_{sc} electrically independent three-phase elementary drives. $\mathbf{X}$ becomes the

vector $\mathbf{X_{dq}}$ in the standard dq-frame whose length is $2N_{sc}$

$$\mathbf{X_{dq}} = \begin{pmatrix} x_{d1} & x_{d2} & x_{d3} & x_{q1} & x_{q2} & x_{q3} \end{pmatrix}^T = \begin{pmatrix} \mathbf{X_d} \\ \mathbf{X_q} \end{pmatrix}. \quad (5)$$

Similarly, in the multiple dq-frame, the inductance matrix is simplified under non-saliency hypothesis as the following $(2N_{sc} \times 2N_{sc})$ matrix

$$[\mathbf{L_{dq}}] = \begin{pmatrix} [\mathcal{L}_{dq}] & [0] \\ [0] & [\mathcal{L}_{dq}] \end{pmatrix}, \quad (6)$$

where $[\mathcal{L}_{dq}]$ is a symmetric $(N_{sc} \times N_{sc})$ matrix containing the self inductances $L_{dq,i}$ of the three-phase elementary drive indexed i and the mutual inductances $M_{dq,ij}$ between the elementary drives i and j

$$[\mathcal{L}_{dq}] = [\mathcal{L}_d] = [\mathcal{L}_q] = \begin{pmatrix} L_{dq,1} & M_{dq,12} & M_{dq,13} \\ M_{dq,21} & L_{dq,2} & M_{dq,23} \\ M_{dq,31} & M_{dq,32} & L_{dq,3} \end{pmatrix}. \quad (7)$$

These terms have to be assessed in the MSS and HCS layouts in order to show the limit of the MDQF control method applied to the proposed HCS structure.

C. Control comparison of the MSS and HCS structures

In order to compare the two segmentation processes described in Fig. 3, an already existing three-phase HEFSM has been rewound with $N_{sc} = 3$ coils per phase per sector. Each coil has dedicated terminals enabling the implementation of either the MSS or HCS configurations (Fig. 3). Both structures are powered similarly by N_{sc} independent inverters (Fig. 2).

As the hybrid excitation of the motor is not exploited in this article, the excitation current remains constant at its rated value for all experiments. Moreover, the saliency of this motor is under 5 %. Hence, it is considered as a simple non-salient three-phase permanent magnet synchronous motor.

Inductance measurements are performed on each sub-winding of each phase for both configurations. As an example, $[\mathcal{L}_a]$ and $[\mathcal{M}_{ab}]$ are shown in Fig. 4 and 5 for the MSS and HCS segmentation approaches, respectively. The inductance values corresponding to different sectors present discrepancies even though their conductors are arranged in a similar way (Fig. 4a). This is caused by disparities in the magnetic circuit. The rotor and the stator may have a small concentricity defect, technically inducing small discrepancies in the air-gap thickness from one sector to another. As far as the HCS windings are concerned, such discrepancies have no impact on their inductance values since they have a symmetrical configuration around the motor.

The coupling factor between i and j sub-windings is defined as

$$k_{ij} = M_{ij}/\sqrt{L_i L_j}. \quad (8)$$

Obviously, the MSS structure has low negative mutual inductance values between the sub-windings belonging to different sectors. As shown in Fig. 4a, the resulting coupling factor between two coils of the same phase is lower than 10 %. Conversely, the HCS structure shows high positive mutual inductances between sub-windings of the same phase, namely with a coupling factor higher than 90 % (Fig. 5a). Note that,

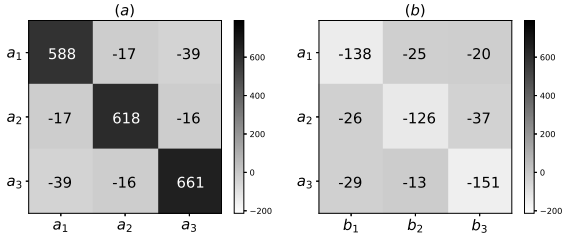

Fig. 4: Inductance values of the prototype with the MSS layout (a) $[\mathcal{L}_s]$ and (b) $[\mathcal{M}_s]$ inductance sub-matrices (μH).

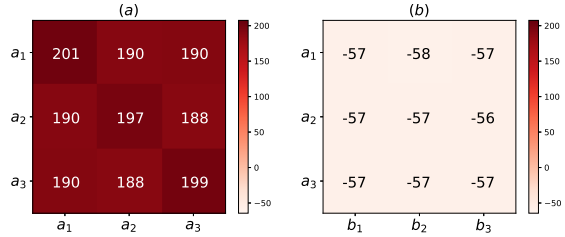

Fig. 5: Inductance values of the prototype with the HCS layout (a) $[\mathcal{L}_s]$ and (b) $[\mathcal{M}_s]$ inductance sub-matrices (μH).

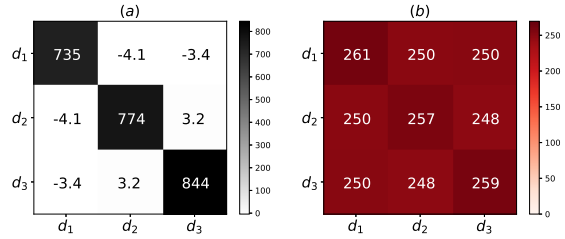

Fig. 6: Comparison of $[\mathcal{L}_{dq}]$ in (a) the MSS and (b) the HCS layouts (μH). Results are equivalent following d and q axes.

within one elementary drive, the coupling factor of two sub-windings (e.g. a_1 and b_1) is close to 25 % for both the MSS and the HCS structures (Fig. 4b and 5b).

Based on the previous inductance measurements, the resulting $[\mathcal{L}_{dq}]$ matrix is computed and depicted in Fig. 6a and 6b for the MSS and HCS structures, respectively. Regarding the MSS approach, the mutual inductances values in the multiple dq-frame are negligible compared with the self inductances ones (Fig. 6a). Conversely, for the HCS approach, the mutual inductances values of the $[\mathcal{L}_{dq}]$ matrix are in the same order of magnitude than the self inductances ones (Fig. 6b). Obviously, these properties impact the control structure.

Fig. 7 illustrates the general control scheme of the segmented HEFSM and clarifies the chosen notations. As the current is accurately measured to be efficiently tracked, equation (9) shows that the control law should integrate feedforward terms to improve the controller dynamic performance:

$$\mathbf{V_{dq}} = R\,\mathbf{I_{dq}} + [\mathbf{L_{dq}}]\,\frac{d}{dt}\begin{pmatrix} \mathbf{I_d} \\ \mathbf{I_q} \end{pmatrix} + \mathbf{E_{dq}} + \Omega_e\,[\mathbf{L_{dq}}]\begin{pmatrix} -\mathbf{I_q} \\ \mathbf{I_d} \end{pmatrix}. \quad (9)$$

The last term is particularly useful since it permits to fully decouple the d and q axes. However, this compensation term is only effective if the non-diagonal terms (i.e. the

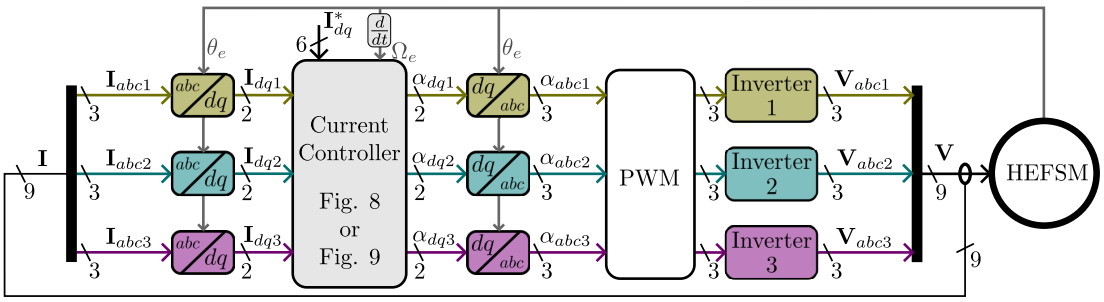

Fig. 7: General control structure of the HEFSM with $N_{sc} = 3$ elementary drives.

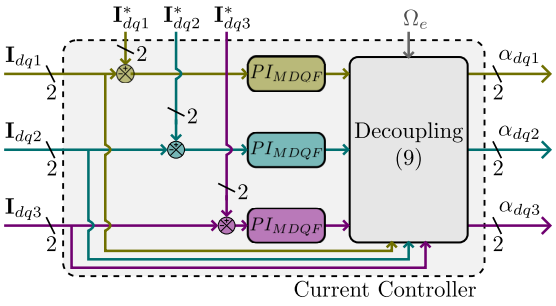

Fig. 8: Current controller implementing the MDQF method with the same PI regulator on each component.

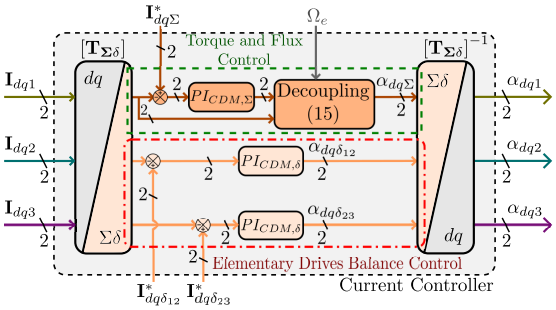

Fig. 9: Current controller implementing the proposed CDM method with specific PI regulator for Σ and δ components.

mutual inductances) are precisely known. As a matter of fact, the poor MSS layout coupling makes possible to choose the standard MDQF control architecture (Fig. 8) where the *Decoupling* block refers to this feedforward term. However, the HCS layout strong positive coupling makes the MDQF control law ineffective regarding the decoupling purpose. Consequently, the suggested approach consists in finding a new frame enabling a good decoupling of the related components. Besides, the adopted transform should not rely on the machine parameters knowledge. Based on these key ideas, the Common and Differential Modes (CDM) control law is proposed and its scheme is given in Fig. 9. The following section gives an in-depth description of the CDM control architecture guidelines and assesses its relevancy based on additional FEA.

III. DQ-BASED CDM CONTROL ARCHITECTURE

A. Additional dq-based transform

As for any 3-phase motor, the standard synchronous dq-frame remains the right option to impose the desired torque and magnetic flux references. However, the HCS structure is characterized by high magnetic coupling between the elementary winding sets. Consequently determining relevant dq-based variables is a key issue to comprehensively control the HCS structure. In the perfect scenario, the latter would

1) have a direct link with the torque/flux as well as the internal power transmission variables.
2) ensure a proper decoupling permitting to switch a $2N_{sc}$ MIMO system into $2N_{sc}$ SISO systems.

The key idea is to exhibit the main physical dynamics of the segmented machine, namely the rapid modes linked to the leakage inductances and the slow mode related to the self and mutual inductances. Additionally, to maintain a proper decoupling between torque and flux variables, the suggested additional transform, named $[\mathbf{T_{\Sigma\delta}}]$ treats independently the d and q axes. It can then be written as

$$[\mathbf{T_{\Sigma\delta}}] = \begin{pmatrix} [\mathcal{T}_d] & [0] \\ [0] & [\mathcal{T}_q] \end{pmatrix} = \begin{pmatrix} [\mathcal{T}] & [0] \\ [0] & [\mathcal{T}] \end{pmatrix} \tag{10}$$

where $[\mathcal{T}]$ is the $(N_{sc} \times N_{sc})$ matrix applied equally to the d and q axes and defined as

$$[\mathcal{T}] = \begin{pmatrix} 1 & 1 & 1 \\ 1 & -1 & 0 \\ 0 & 1 & -1 \end{pmatrix}. \tag{11}$$

Transformation (10) is applied to $\mathbf{X_{dq}}$ (5), thus leading to $\mathbf{X_{\Sigma\delta}}$, the $2N_{sc}$-component vector in the suggested $\Sigma\delta$-frame. It is structured as follows:

$$\mathbf{X_{\Sigma\delta}} = [\mathbf{T_{\Sigma\delta}}] \cdot \mathbf{X_{dq}} = \begin{pmatrix} x_{d\Sigma} & \mathbf{X}_{d\delta} & x_{q\Sigma} & \mathbf{X}_{q\delta} \end{pmatrix}^T. \tag{12}$$

The first component $x_{d\Sigma}$ is named common mode variable of the d-axis. The remaining two components, $x_{d\delta 12}$ and $x_{d\delta 23}$, included in $\mathbf{X}_{d\delta}$, are the differential mode variables of the d-axis and reflect the difference between two elementary drives. Similar reasoning applies on the q-axis.

A FEA assessment justifies the relevancy of this choice. Indeed, the basis for this approval is typically that the HCS sub-windings are located around the same stator tooth and hence embrace almost the same flux lines. The FEA study is carried out using Ansys Maxwell 2D software and it is applied

on the HCS winding configuration (Fig. 3b). First, the test sets a non-zero common mode current for the $N_{sc} = 3$ sub-windings of phase a, setting the 2 differential mode currents to zero. Fig. 10a shows the resulting magnetic field lines. They cross radially the rotor-stator air-gap and hence impact the interaction of magnetic flux between both mechanical parts and leads to an electromagnetic torque. Moreover, as by design, the air-gap thickness is very small, the common mode inductance value is large. It results that the common mode dynamic is low. Second, the two other numerical experiments enforce a non-zero differential mode current. Fig. 10b and 10c exhibits the corresponding magnetic field lines which obviously remain located in the stator. They solely cross the stator slots, thicker than the air-gap. As a result, the differential mode inductance value is much lower than the common mode one. It proves that the dynamics of the common and differential modes are highly different and should be accounted for separately. Besides, based on the FEA, it is also clear that the differential currents have no impact on either the air-gap magnetic flux or the machine torque. They mainly modify the power sharing between elementary drives.

B. Impact on the inductance matrix

The common and differential modes transformation $[\mathcal{T}]$ is applied to the inductance matrix obtained in (7). It derives:

$$[\mathcal{L}_{\Sigma\delta}] = [\mathcal{T}] \cdot [\mathcal{L}_{dq}] \cdot [\mathcal{T}]^{-1} = \begin{pmatrix} L_\Sigma & \mathbf{L}_{\Sigma\delta} \\ \mathbf{L}_{\delta\Sigma} & [\mathcal{L}_\delta] \end{pmatrix}. \tag{13}$$

The inductance matrix in the dq-based $\Sigma\delta$ frame is computed either using the FEA or the previous inductance measurements performed on the HCS prototype (Fig. 11). Although the 2D assumption slightly overestimates the various coupling impacts, both results are clearly consistent. They confirm the previous FEA assessment based on physical considerations. They lead to the conclusion that:

1) The differential modes has no impact on the air-gap magnetic flux and the electromagnetic torque ($d\Sigma$ and $q\Sigma$ modes, respectively). Accordingly the $[\mathcal{L}_{\Sigma\delta}]$ inductance matrix could be simplified as:
$$[\mathcal{L}_{\Sigma\delta}] = \begin{pmatrix} L_\Sigma & [0] \\ \mathbf{L}_{\delta\Sigma} & [\mathcal{L}_\delta] \end{pmatrix}. \tag{14}$$
2) The common mode dynamic is imposed by the L_Σ value which is very large in comparison with the other terms of the related matrix.
3) Each differential mode has small inductances compared to L_Σ (hundred times smaller), leading to a relative high dynamic with regard to the common mode one.
4) The common mode slightly impacts the differential ones. Moreover, since the former dynamics is very slow in comparison to the latter one, the differential mode controller easily reject this perturbation.

C. HCS dedicated controller

Combining (9), (12) and (14), the common mode components are governed by

$$\begin{cases} v_{d\Sigma} = R \cdot i_{d\Sigma} + L_\Sigma \cdot \frac{di_{d\Sigma}}{dt} + e_{d\Sigma} - \Omega_e \cdot L_\Sigma \cdot i_{q\Sigma} \\ v_{q\Sigma} = R \cdot i_{q\Sigma} + L_\Sigma \cdot \frac{di_{q\Sigma}}{dt} + e_{q\Sigma} + \Omega_e \cdot L_\Sigma \cdot i_{d\Sigma} \end{cases} \tag{15}$$

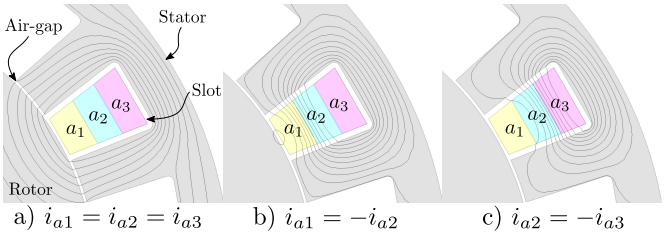

Fig. 10: Flux lines without excitation around three sub-windings of phase a in the HCS structure (Fig. 3b) for the common and differential components defined by (11).

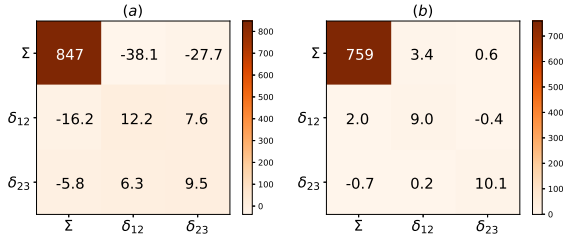

Fig. 11: Comparison of $[\mathcal{L}_{\Sigma\delta}]$ (μH) obtained through a) FEA and b) the inductance measurements of the HCS approach shown in Fig. 6b. Results are equivalent following d and q axes.

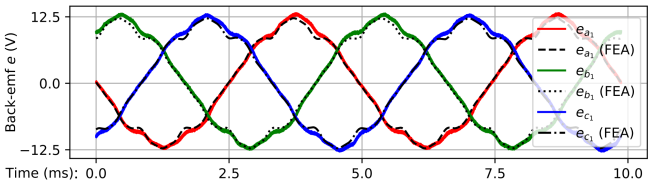

Fig. 12: Comparison of back electromotive force measurements and FEA results. ($\hat{E} = 12.5\ V$, $f_e = 200\ Hz$).

TABLE II: HCS back-emf $\Sigma\delta$ components ($f_e = 200Hz$)

	Experimental	FEA
$e_{q\Sigma}$	$37.5\ V$	$37.5\ V$
$e_{q\delta 12}$	$35\ mV$	$23\ mV$
$e_{q\delta 23}$	$15\ mV$	$10\ mV$

where $e_{d\Sigma}$ and $e_{q\Sigma}$ represent the back emf due to permanent magnets and excitation coils along the Σ-axis.

To achieve an effective transient decoupling of $d\Sigma$ and $q\Sigma$ components, it is crucial to combine the feedback action with a specific feedforward term. Fig. 9 shows this additional term as a *Decoupling* block permitting to compensate the last terms of (15). Apart from measuring the rotor speed and the sub-winding currents, the compensation term only requires the knowledge of L_Σ value. Moreover, the two differential modes are independently controlled (Fig. 9). Indeed, the measured inductance matrix is practically diagonal (Fig. 11b) while the common component current evolves slowly and is hence easily rejected by the feedback term.

Furthermore, the 2D FEA model also enables to compute the back-emf which is then compared to the no-load voltages measured on the prototype in its HCS configuration (Fig. 3b).

TABLE III: PI Controllers tuning
(10 dB gain margin and 60 $^\circ$ phase margin criteria)

	r (Ω)	l (μH)	$\tau = \frac{l}{r}$ (ms)	K_p (10^{-3})	T_i (ms)
MDQF,Σ	0.2	760	3.8	2.1	1.24
MDQF,δ	0.2	10	0.05		
CDM,Σ	0.2	760	3.8	100	4.0
CDM,δ	0.2	10	0.05	1.4	0.05

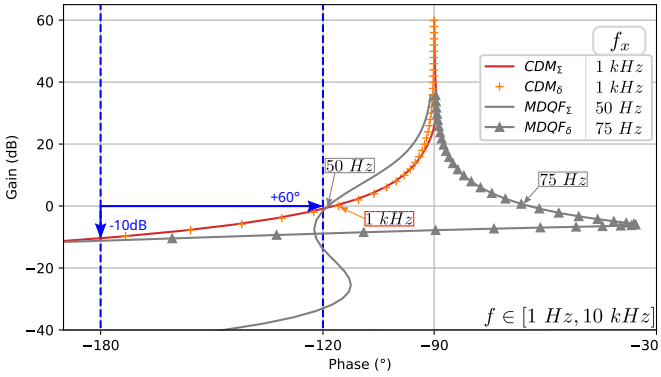

Fig. 13: Open-loop transfer function Nichols plot for the MDQF and CDM tuning parameters described in Table III.

These estimated variables are actually consistent with the real voltages measured in the HCS structure (Fig. 12). Moreover, Table II shows that the two differential mode components of $\mathbf{E}_\delta$ are thousand times lower than the common mode one. Hence, feeding each elementary drive with an equal current set point yields to a similar electromagnetic torque contribution.

For comparative purposes, the PI parameters of the standard MDQF technique (Fig. 8) and the proposed CDM method (Fig. 9) have been tuned based on the same specifications. The PI regulators settings should provide 10 dB-60 $^\circ$ gain-phase margins while maximizing the open-loop gain crossover frequency f_x. Assuming that for both cases, the plant is sufficiently well decoupled by the aforementioned feedforward compensation terms (9), the relation between the duty cycle α and the related current i is given by a first order system (r, l) associated with a pure delay. The latter includes both the computational delay of the microcontroller equal to one sampling period and the stochastic delay induced by the digital PWM. Denoting $T_s = 50\mu s$ the control sampling time, the global delay to be considered is therefore equal to $1.5 \times T_s$. Consequently, the SISO system transfer function to be regulated is as follows:

$$H(s) = \frac{I(s)}{\alpha(s)} = \frac{V_{DC} \cdot e^{-1.5 \cdot T_s \cdot s}}{r + l \cdot s} \tag{16}$$

with $V_{DC} = 48V$ the DC-link voltage of the segmented power supply, r the winding resistance and l the considered inductance. This latter could be either L_Σ or L_δ. In the proposed CDM controller, each of the common (Σ) and differential (δ) components benefit from a specific PI parameter setting whereas in the MDQF controller, the PI parameter setting acts on both components without distinction. In all cases, the open-loop transfer function in Σ or δ component can be written as:

$$H_{OL}(s) = K_p \cdot \left(1 + \frac{1}{T_i \cdot s}\right) \cdot H(s) \tag{17}$$

where K_p and T_i are the proportional gain and the integral time constant of the PI. Based on the $[\mathcal{L}_{\Sigma\delta}]$ values listed in Fig. 11b, the CDM parameter sets of the Σ and δ are adjusted as shown in Table III. It results in the same Σ and δ open-loop frequency response as depicted in Fig. 13 (CDM, Σ and CDM, δ). The resulting gain crossover frequency is $f_{x,\Sigma\delta} = 1\ kHz$.

However, the MDQF method imposes, because of the intrinsic structure of such controller (Fig. 8), that the PI parameter setting is unique and therefore, affects both the common (Σ) and differential (δ) components. It is then necessary to choose the best trade-off which maximizes the bandwidth of the Σ component with a phase margin of at least 60 $^\circ$ and at the same time do not degrade too much the stability on the δ axis (phase margin$>$ 60 $^\circ$ and gain margin$>$ 10 dB). Thus, this unique parameter set induces a lower bandwidth for the Σ component ($f_{x,\Sigma} = 50\ Hz$) compared to what was obtained with the CDM method, resulting in a larger settling time. The δ component cross-frequency is also low in order to ensure the 10 dB gain margin ($f_{x,\delta} = 75\ Hz$). Fig. 13 ($MDQF, \Sigma$ and $MDQF, \delta$) shows the related open-loop frequency responses and the adopted PI parameters are given in Table III.

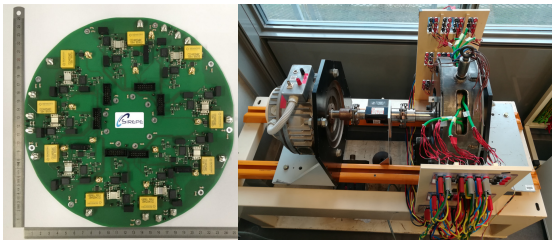

Fig. 14: View of the triple three-phase inverter (left) and the HEFSM motor with HCS layout (right).

IV. Experimental Results

To validate the proposed controller, an experimental setup has been implemented (Fig. 14). The synchronous motor described in section II is configured in the HCS structure and driven by $N_{sc} = 3$ basic 3-phase inverters. The latter, located on the same Printed Circuit Board (PCB) are powered by a common 48 V DC source and their switching frequency is set at $F_s = 20\ kHz$. The aforementioned control laws are implemented in a dSpace MicroLabBox and the sampling frequency is synchronized with the switching one. In addition, a DC motor imposes a controlled load torque.

The purpose of the following experiments is to highlight the relevancy of the proposed CDM control compared to the standard MDQF method initially developed to drive MSS motor structures. It also aims at demonstrating the capability to drive the HCS motor structure at any speed and to enforce any power distribution reference even in case of faulty operation.

A. Control Methods Comparison for the HCS Structure

The first test consists in enforcing torque setpoint steps from its rated value to 0, and vice-versa between 0 ms and

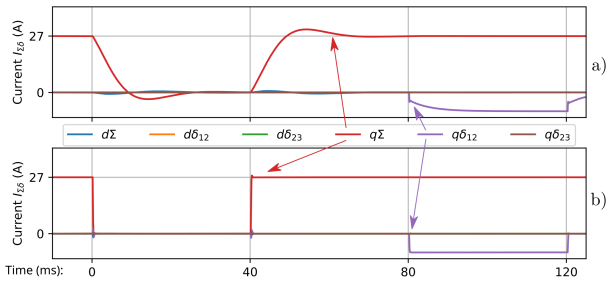

Fig. 15: Simulation results at $N = 600\ rpm$ with a) the MDQF control and b) the proposed CDM control.

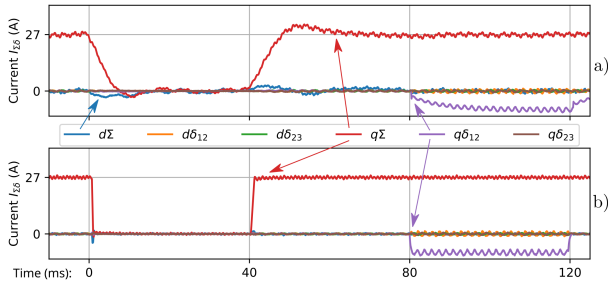

Fig. 16: Experimental results at $N = 600\ rpm$ with a) the MDQF control and b) the proposed CDM control.

$40\ ms$. Meanwhile, the rotor speed is maintained constant by controlling the load torque. Both differential references are set to zero: $\mathbf{I}^*_{d\delta} = 0$ and $\mathbf{I}^*_{q\delta} = 0$. Then, a step response occurs on the $q\delta 12$ component between $80\ ms$ and $120\ ms$ in order to validate the differential mode controller design. The test has been implemented in simulation (Fig. 15) using MATLAB/Simulink software. Worth to be mentioned here, the control feedforward terms used in this simulation are ideal since they perfectly match their actual counterparts (Fig. 6b and (9)).

First, the simulation results fully validate the predictions based on the open-loop frequency response. The standard MDQF method shows poor performances (Fig. 15a). The q-axis common mode current component ($i_{q\Sigma}$) exhibits a significant overshoot and a long settling time ($\approx 20\ ms$) which is consistent with its low computed open-loop cross frequency ($\approx 50\ Hz$). This overshoot may lead to exceed the acceptable current limit in one of the elementary drives. Similarly, the δ-axis settling time also proves to be large, which is in line with its reduced bandwidth (Fig. 13). Conversely the suggested CDM control structure exhibits good and similar performances regarding either $i_{q\Sigma}$ or $i_{q\delta 12}$ (Fig. 15b). It also highly mitigates the overshoot on the $q\Sigma$-axis. Each component features the same $1\ ms$ settling time, which is fully consistent with the computed $1\ kHz$ open-loop cross frequency (Fig. 13).

Second, the same test is then experimentally done. An anti-windup method is implemented on the duty-cycle values and, as it is on the actual system, only approximated parameters are used in the feedforward action (Fig. 16). As can be seen, the experimental waveforms are in close agreement with the simulation results (Fig. 15). In all measurements,

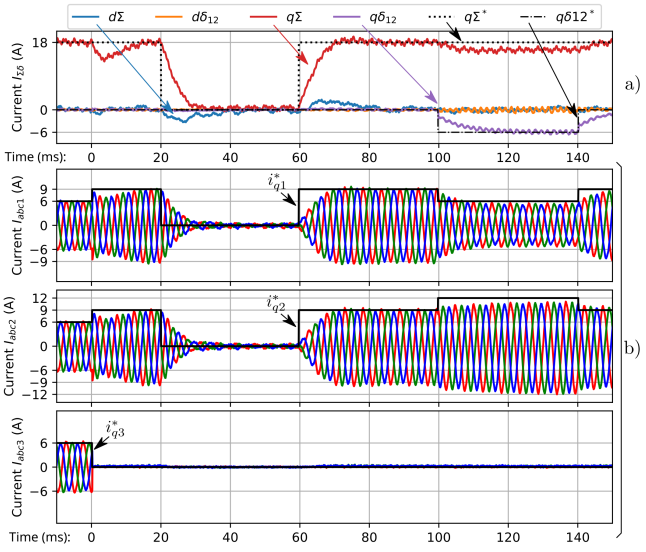

Fig. 17: Measured a) $\Sigma\delta$ and b) sub-winding currents during $q\Sigma$ and $q\delta 12$ steps under $abc3$ elementary drive deactivation with the standard MDQF control.

the residual ripples on $i_{q\Sigma}$ are due to the non-sinusoidal waveforms of back-emf (Fig. 12). Apart from that, a few other differences and similarities are worth to be mentioned. Regarding the standard MDQF technique, the measured d-axis common mode current component ($i_{d\Sigma}$) is deeply impacted by the $i_{q\Sigma}$ transient (Fig. 16a), which negatively induces a magnetic field transient in the air-gap. Indeed, in practice, the feed forward compensation terms (9) imperfectly compensates the coupling terms, since these terms are based on measurements of mutual inductances that are of course affected by uncertainties. Conversely, CDM approach presents very small discrepancies between simulation and experimental results. Even though the q-axis dynamics is slowed by the brief duty-cycle value saturation during transient, it is more than ten times faster than the the results obtained with the MDQF method. Moreover, using the CDM method, the d-axis common mode component is not impacted by the q-axis Σ component transient since it remains equal to zero (Fig. 16b). This proves that the dq axes decoupling remains efficient even though affected by measurement uncertainties. Indeed, the additional $\Sigma\delta$ transform used in the CDM control method permits to base the feedforward compensation term on a single measurement, namely L_Σ. This latter measurement is truly quite easy to perform correctly.

Finally, the proposed CDM method is well adapted to drive a HCS structure. Since this method also improves the differential component control, it opens up the possibility to consider for future works the power-sharing between the different elementary drives.

B. Faulty Operation

A second test is performed to illustrate the promising abilities of the HCS structure controlled with both the standard MDQF method (Fig. 17) and the proposed CDM method (Fig. 18). For both control methods, one of the three inverters is suddenly turned off at $0\ ms$ while keeping $i^*_{q\Sigma}$ constant to

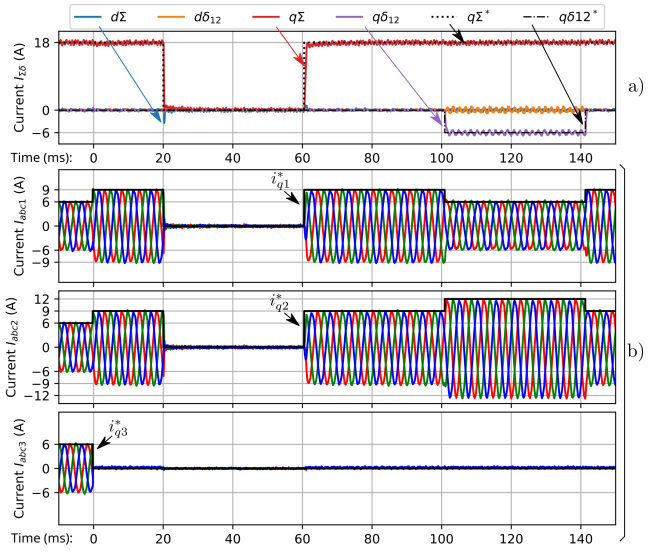

Fig. 18: Measured a) $\Sigma\delta$ and b) sub-winding currents during $q\Sigma$ and $q\delta 12$ steps under $abc3$ elementary drive deactivation with the proposed CDM control.

$18\ A$. This configuration corresponds to an open-winding fault operation. Then, the common mode component setpoint $i^*_{q\Sigma}$ is set to $0\ A$ between $20\ ms$ and $60\ ms$ and the remaining differential component setpoint $i^*_{q\delta 12}$ is set to $-6\ A$ between $100\ ms$ and $140\ ms$. These two step responses evaluate the fault ride through capacity of the structure.

Using the MDQF method, the common component (Σ) is deeply affected by the open-winding fault and the differential component step response interferes with the common component behavior (Fig. 17). This is mainly due to the poor dynamical performances of the MDQF control, described in Fig. 13. Conversely, using the CDM method, the torque control remains effective even when only two out of three elementary drives are operating (Fig. 18a). Additionally, the power-sharing between the two remaining elementary drives is still operational since the differential component control can still be realized in such degraded mode (Fig. 18b).

V. Conclusions and Perspectives

The novel stator winding segmentation process studied in this article enables to supply an electric machine with a reduced DC-link voltage without changing its operational range or increasing the rated current of the feeding inverters. With its multiple degrees of freedom and high magnetic couplings, this attractive topology offers important control challenges which the present study addresses. The scope of the current contribution is limited to designing a proof of concept based on an existing three-phase machine configured as a segmented three-phase motor facing high positive magnetic coupling between each elementary drives. The developed approach consists in extending the standard dq transform with a common and differential modes transform. A comprehensive dynamical model is developed using analytical equations and FEA method. It shows that the extended transformation is suitable to easily track the control objectives, i.e. the global machine operating point (the torque and air-gap magnetic field) while ensuring a balanced power distribution between all the elementary drives. An experimental setup has been developed. The experiments show that the aforementioned model is reliable, enabling to tune properly the control parameters. The stability enhancement provided by the proposed CDM control method compared to the standard MDQF technique has been shown. Moreover, the CDM control architecture can enforce balanced power distribution between elementary drives whatever the electric machine operating point and even under open-fault condition. As a consequence, the elementary drive power allocation ability seems to be an interesting opportunity for future research lines.

Appendix

- HCS: *Highly Coupled Segmentation*
- MSS: *Multi-Sector Segmentation*
- MDQF: *Multiple dq-Frame*
- CDM: *Common and Differential Modes*
- MK3P: *Multiphase with $k \times 3$ Phases*
- FEA: *Finite Element Analysis*
- HEFSM: *Hybrid Excitation Flux Switching Machine*

References

[1] C. Zoeller, T. M. Wolbank, and M. A. Vogelsberger, "Inverter-fed drive stator insulation monitoring based on reflection phenomena stimulated by voltage step excitation," *ECCE 2016 - IEEE Energy Conversion Congress and Exposition, Proceedings*, DOI 10.1109/ECCE.2016.7855213, no. 838478, pp. 1–8, 2016.

[2] M. Ghassemi, "Accelerated insulation aging due to fast, repetitive voltages: A review identifying challenges and future research needs," *IEEE Transactions on Dielectrics and Electrical Insulation*, vol. 26, DOI 10.1109/TDEI.2019.008176, no. 5, pp. 1558–1568, 2019.

[3] J. Wang, Y. Li, and Y. Han, "Integrated Modular Motor Drive Design With GaN Power FETs," *IEEE Transactions on Industry Applications*, vol. 51, DOI 10.1109/tia.2015.2413380, no. 4, pp. 3198–3207, 2015.

[4] F. Maislinger, H. Ertl, G. Stojcic, C. Lagler, and F. Holzner, "Design of a 100 kHz wide bandgap inverter for motor applications with active damped sine wave filter," *The Journal of Engineering*, vol. 2019, DOI 10.1049/joe.2018.8059, no. 17, pp. 3766–3771, 2019.

[5] C. Alosa, F. Immovilli, and E. Lorenzani, "Modular Multi-Three-Phase Electric Drives for Enhanced Reliability and Current Ripple Minimization," *IECON Proceedings (Industrial Electronics Conference)*, DOI 10.1109/IECON.2019.8927819, pp. 7108–7114, 2019.

[6] G. Sala, G. Valente, M. D. Nardo, M. Degano, P. Zanchetta, and C. Gerada, "Power-Sharing Control in Bearingless Multi-Sector and Multi-Three-Phase Permanent Magnet Machines," *IEEE Transactions on Industrial Electronics*, vol. 68, DOI 10.1109/TIE.2020.3026273, no. 10, pp. 9070–9080, 2021.

[7] B. Rubey, A. Patzak, F. Bachheibl, A. Greifelt, and D. Gerling, "Lifetime estimation of a novel high current low resistance single phase plug-in connector for the ISCAD application," *14th Brazilian Power Electronics Conference, COBEP 2017*, vol. 2018-Janua, DOI 10.1109/COBEP.2017.8257246, pp. 1–5, 2017.

[8] A. H. Mohamed, H. Vansompel, and P. Sergeant, "Design of an Integrated DC-Link Structure for Reconfigurable Integrated Modular Motor Drives," *IEEE Transactions on Industrial Electronics*, vol. 0046, DOI 10.1109/TIE.2021.3065620, no. c, 2021.

[9] R. Abebe, G. Vakil, G. L. Calzo, T. Cox, S. Lambert, M. Johnson, C. Gerada, and B. Mecrow, "Integrated motor drives: State of the art and future trends," *IET Electric Power Applications*, vol. 10, DOI 10.1049/iet-epa.2015.0506, no. 8, pp. 757–771, 2016.

[10] L. Verkroost, J. Van Damme, D. V. Bozalakov, F. De Belie, P. Sergeant, and H. Vansompel, "Simultaneous DC-Link and Stator Current Ripple Reduction with Interleaved Carriers in Multiphase Controlled Integrated Modular Motor Drives," *IEEE Transactions on Industrial Electronics*, vol. 68, DOI 10.1109/TIE.2020.2992965, no. 7, pp. 5616–5625, 2021.

[11] E. Hoang and E. Labouré, "Electric machine supplied at low voltage and associated multicellular power train," Nov. 28 2019, US20190363599A1. [Online]. Available: https://patentscope.wipo.int/search/fr/detail.jsf?docId=US277543730

[12] A. Cizeron, J. Ojeda, E. Labouré, and O. Béthoux, "Prediction of PWM-induced current ripple in subdivided stator windings using admittance analysis," *Energies*, vol. 12, DOI 10.3390/en12234418, Nov. 2019.
[13] H. J. Raherimihaja, Q. Zhang, G. Xu, and X. Zhang, "Integration of Battery Charging Process for EVs into Segmented Three-Phase Motor Drive with V2G-Mode Capability," *IEEE Transactions on Industrial Electronics*, vol. 68, DOI 10.1109/TIE.2020.2978684, no. 4, pp. 2834–2844, 2021.
[14] S. Rubino, O. Dordevic, R. Bojoi, and E. Levi, "Modular Vector Control of Multi-Three-Phase Permanent Magnet Synchronous Motors," *IEEE Transactions on Industrial Electronics*, vol. 68, DOI 10.1109/TIE.2020.3026271, no. 10, pp. 9136–9147, 2021.
[15] D. Golovanov, D. Gerada, G. Sala, M. Degano, A. Trentin, P. H. Connor, Z. Xu, A. L. Rocca, A. Galassini, L. Tarisciotti, C. N. Eastwick, S. J. Pickering, P. Wheeler, J. Clare, M. Filipenko, and C. Gerada, "4-MW Class High-Power-Density Generator for Future Hybrid-Electric Aircraft," *IEEE Transactions on Transportation Electrification*, vol. 7, DOI 10.1109/TTE.2021.3068928, no. 4, pp. 2952–2964, 2021.
[16] Z. Zhu, S. Wang, B. Shao, L. Yan, P. Xu, and Y. Ren, "Advances in dual-three-phase permanent magnet synchronous machines and control techniques," *Energies*, vol. 14, DOI 10.3390/en14227508, no. 22, 2021. [Online]. Available: https://www.mdpi.com/1996-1073/14/22/7508
[17] G. Sala, M. Mengoni, G. Rizzoli, M. Degano, L. Zarri, and A. Tani, "Impact of Star Connection Layouts on the Control of Multiphase Induction Motor Drives under Open-Phase Fault," *IEEE Transactions on Power Electronics*, vol. 36, DOI 10.1109/TPEL.2020.3024205, no. 4, pp. 3717–3726, 2021.
[18] S. Rubino, O. Dordevic, E. Armando, I. R. Bojoi, and E. Levi, "A Novel Matrix Transformation for Decoupled Control of Modular Multiphase PMSM Drives," *IEEE Transactions on Power Electronics*, vol. 36, DOI 10.1109/TPEL.2020.3043083, no. 7, pp. 8088–8101, 2021.
[19] C. C. Lin and Y. Y. Tzou, "An innovative multiphase PWM control strategy for a PMSM with segmented stator windings," *Conference Proceedings - IEEE Applied Power Electronics Conference and Exposition - APEC*, vol. 2015-May, DOI 10.1109/APEC.2015.7104362, no. May, pp. 270–275, 2015.
[20] H. H. Hsu and Y. Y. Tzou, "FPGA control and implementation of a multiphase-interleaved PWM inverter for a segmented PMSM," *Proceedings of the International Conference on Power Electronics and Drive Systems*, vol. 2015-Augus, DOI 10.1109/PEDS.2015.7203410, no. June, pp. 224–230, 2015.
[21] D. Jiang, K. Liu, Z. Liu, Q. Wang, Z. He, and R. Qu, "Four-Module Three-Phase PMSM Drive for Suppressing Vibration and Common-Mode Current," *IEEE Transactions on Industry Applications*, vol. 57, DOI 10.1109/TIA.2021.3085542, no. 5, pp. 4874–4883, 2021.
[22] G. Sala, G. Valente, D. Gerada, P. Zanchetta, and C. Gerada, "Post-Fault Operation of Bearingless Multisector SPM Machines by Space Vector Control," *IEEE Transactions on Power Electronics*, vol. 35, DOI 10.1109/TPEL.2019.2933922, no. 4, pp. 4168–4177, 2020.
[23] Y. Hu, Z. Q. Zhu, and M. Odavic, "Comparison of Two-Individual Current Control and Vector Space Decomposition Control for Dual Three-Phase PMSM," *IEEE Transactions on Industry Applications*, vol. 53, DOI 10.1109/TIA.2017.2703682, no. 5, pp. 4483–4492, 2017.
[24] W. Zhang, Y. Xu, H. Huang, and J. Zou, "Vibration reduction for dual-branch three-phase permanent magnet synchronous motor with carrier phase-shift technique," *IEEE Transactions on Power Electronics*, vol. 35, DOI 10.1109/TPEL.2019.2910311, no. 1, pp. 607–618, 2020.
[25] G. Wu, S. Huang, Q. Wu, F. Rong, C. Zhang, and W. Liao, "Robust Predictive Torque Control of Nx3-Phase PMSM for High-Power Traction Application," *IEEE Transactions on Power Electronics*, vol. 35, DOI 10.1109/TPEL.2020.2981914, no. 10, pp. 10 799–10 809, 2020.
[26] X. Wang, G. Sala, H. Zhang, C. Gu, G. Buticchi, A. Formentini, C. Gerada, and P. Wheeler, "Torque Ripple Reduction in Sectored Multi Three-Phase Machines Based on PWM Carrier Phase Shift," *IEEE Transactions on Industrial Electronics*, vol. 67, DOI 10.1109/TIE.2019.2931239, no. 6, pp. 4315–4325, 2020.
[27] H. Zhang, P. Giangrande, G. Sala, Z. Xu, W. Hua, V. Madonna, D. Gerada, and C. Gerada, "Thermal Model Approach to Multisector Three-Phase Electrical Machines," *IEEE Transactions on Industrial*
[28] H. Ben Ahmed, L. Béthoux, A. Cizeron, E. Hoang, A. Juton, E. Labouré, A. Mercier, E. Monmasson, J. Ojeda, L. Queval, and G. Remy, "Electric Traction Chain with Segmented Power Supply," *23rd European Conference on Power Electronics and Applications (EPE21 ECCE Europe)*, Sep. 2021.
Electronics, vol. 68, DOI 10.1109/TIE.2020.2977559, no. 4, pp. 2919–2930, 2021.
[29] Q. Zhang, H. J. Raherimihaja, G. Xu, and X. Zhang, "Design and Performance Analysis of Segmented Three-Phase IPMSM for EVs Integrated Battery Charger," *IEEE Transactions on Industrial Electronics*, vol. 68, DOI 10.1109/TIE.2020.3021642, no. 10, pp. 9114–9124, 2021.
[30] D. W. Chung, J. S. Kim, and S. K. Sul, "Unified voltage modulation technique for real-time three-phase power conversion," *IEEE Transactions on Industry Applications*, vol. 34, DOI 10.1109/28.663482, no. 2, pp. 374–380, 1998.

Antoine Cizeron received the MSc degree in electrical engineering from Université Paris-Saclay in 2019. Since then, he has been working toward the Ph. D. degree in the Group of electrical engineering - Paris (GeePs, UMR CNRS 8507) and the Systèmes et Applications des Technologies de l'Information et de l'Energie laboratory (SATIE, UMR CNRS 8029). His current research interests include modeling and control of motor drives.

Javier Ojeda (M'06) was born in Buenos Aires, Argentina. He received the PhD. degree in electrical engineering from Ecole Normale Supérieure de Cachan, France, in 2009. Since 2010, he is an assistant professor in the Ecole Normale Supérieure Paris-Saclay, SATIE Laboratory and EEA teaching Department. His current research interests include modeling and control of multiphase motors.

Eric Monmasson (M'96-SM'06) received the Ing. and Ph.D. degrees from the Ecole Nationale Supérieure d'Ingénieurs d'Electrotechnique d'Electronique d'Informatique et d'Hydraulique de Toulouse, Toulouse, France, in 1989 and 1993, respectively. Since 2003, he is a Full Professor at the University of Cergy-Pontoise, Cergy-Pontoise, France. He is also with the Systèmes et Applications des Technologies de l'Information et de l'Energie laboratory (SATIE, UMR CNRS 8029), Cergy-Pontoise. He is the author or coauthor of 3 books and more than 200 scientific papers. His current research interests include the control of power electronics, electrical motors and generators, and FPGA-based and SoC-based industrial control systems. Dr. Monmasson was the Chair of the technical committee on Electronic Systems-on-Chip of the IEEE Industrial Electronics Society from 2008 to 2011. He is also a member of the steering committee of the European Power Electronics Association and he was the Chair of the number one technical committee of the International Association for Mathematics and Computers in Simulation (2011-2017). He is an Associate Editor of the IEEE Transactions on Industrial Informatics and the Editor-in-Chief of the IEEE Industrial Electronics Magazine.

Olivier Béthoux received the M.Sc. degree from Ecole Centrale de Lille, Villeneuve-d'Ascq, France, in 1990, and the Ph.D. degree from The University of Cergy-Pontoise, Pontoise, France, in 2005. From 1992 to 1997, he was a Research Engineer with the Alstom Research Center, France. From 1999 to 2017 he has been an Assistant Professor first in the Ecole Nationale d'Electronique et de ses Applications (ENSEA) and then in the Paris-Saclay University, France. Since 2017, he is a Full Professor at the Sorbonne Université, Paris, France. Since 2006, He has also been with the Group of electrical engineering - Paris (GeePs, UMR CNRS 8507), Paris. He is the author or coauthor of 2 books and more than 150 scientific papers. His main research interests include the analysis, design, control, and fault diagnosis of power electronics and electric machines. He is also deeply involved in advanced control techniques and energy management of fuel cells and photovoltaic systems.